Yang, L., Wang, P., **Zhang, S.**, Wang, Y., Zang, L., Zhu, H., Yin, J., Yang, H.Y. (2020):
Flexible and additive-free organic electrodes for aqueous sodium ion batteries
J. Mater. Chem. A **8** (43), 22791 - 22801

http://dx.doi.org/10.1039/d0ta07267b

View Article Online
View Journal

Journal of
Materials Chemistry A

Materials for energy and sustainability

This article can be cited before page numbers have been issued, to do this please use: L. Yang, J. Yin, L. Zang, H. Zhu, P. Wang, S. Zhang, Y. Wang and H. Y. Yang, *J. Mater. Chem. A*, 2020, DOI: 10.1039/D0TA07267B.

ROYAL SOCIETY
OF **CHEMISTRY**

rsc.li/materials-a

View Article Online
DOI: 10.1039/D0TA07267B

Flexible and Additive-Free Organic Electrodes for Aqueous Sodium Ion Batteries

Liping Yang[a], Pengyuan Wang[b], Shangwei Zhang[c], Yuanhao Wang[d], Ling Zang[e], Hui Zhu[a], Jiao Yin[a]*, Hui Ying Yang[f]*

[a] Laboratory of Environmental Sciences and Technology, Xinjiang Technical Institute of Physics & Chemistry, and Key Laboratory of Functional Materials and Devices for Special Environments, Chinese Academy of Sciences, Urumqi 830011, China

[b] School of Physical Science and Technology, Xinjiang University, Urumqi 830046, PR China

[c] UFZ Department of Ecological Chemistry, Helmholtz Centre for Environmental Research, Permoserstraße 15, 04318 Leipzig, Germany

[d] SUSTech Engineering Innovation Center, School of Environmental Science and Engineering, Southern University of Science and Technology

[e] Nano Institute of Utah and Department of Materials Science and Engineering, University of Utah, Salt Lake City, Utah 84112, United States

[f] Pillar of Engineering Product Development, Singapore University of Technology and Design, 8 Somapah Road, Singapore 487372, Singapore

Corresponding author: yinjiao@ms.xjb.ac.cn (J. Yin); yanghuiying@sutd.edu.sg (H. Y. Yang)

Abstract

View Article Online
DOI: 10.1039/D0TA07267B

Organics materials with redox activities are promising candidates for aqueous flexible sodium ion storage devices (AFSISDs) due to their mechanical flexibility and low dissolution in aqueous electrolytes. However, the advantages of organic electrodes are not fully exploited due to uncontrollable morphologies with sluggish electrochemical kinetics, and shortage of deep understanding about storage mechanism via in-situ technologies. Herein, an interfacial self-assembly strategy is proposed to directly construct PTCDI nanofibers onto a flexible ITO substrates by a binder-free approach. Combining the in-situ Raman spectroscopy and DFT calculation, the Na^+ storage mechanism based on enolization reaction (-C=O↔-C-O-Na) of two carbonyl groups located in the para position of PTCDI is illuminated. Coupled with an activated carbon cathode, the organic AFSISD delivers an ultrahigh energy density of 83.8 Wh kg^{-1} and a largely improved power density of 3.4 kW kg^{-1}. The as-prepared organic nanofiles shows a superior volumetric energy and high power density (i.e., 7.1 mWh cm^{-3} and 289.7 mW cm^{-3}). This work opens up new horizons for a wide variety of flexible electronics based on organic electrode materials in aqueous neutral electrolytes.

Keywords: self-assembly, PTCDI nanofibers, flexible sodium-ion storage devices, in-situ Raman spectroscopy, DFT calculations

View Article Online
DOI: 10.1039/D0TA07267B

1. Introduction

The growing demand for wearble electronics devices promote the urgent need of flexible energy storage devices with high energy density, excellent cyclicality and long life span. [1, 2] Sodium-ion batteries (SIBs) have been recognised as one promising alternative to conventional lithium-ion batteries (LIBs) owing to the abundant sodium resources. [3, 4] Searching for flexible suitable electrode materials with high reversible capacity and fast Na^+ ion transport kinetics is vitally important and challenging. The aqueous flexible sodium ion storage devices (AFSISDs) have been featured as an attractive approach because of the integrative device advantages. In the construction of AFSISDs, the aqueous electrolytes are considered to be inherently safer, cheaper and more environmentally friendly than conventional organic counterparts. [5, 6] Organics electrodes have been intensively explored as promising candidates for sodium storage, due to their low cost, abundant resources, excellent structural adaptability and mechanical flexibility. However, most of the orgranic electrodes suffer from poor electrical conductivity and the high dissolution in organic electrolytes. [7, 8] Therefore, effective organics electrodes with high capacity and stabilities have attracted significant amount of research interests. To make effective configuration of AFSISDs, numerous attempts have been proposed to embed organic active materials in flexible conductive substrates, such as carbon nanofibers, carbon nanotubes, graphene derivatives and carbon textiles. [9, 10, 11] However, the mass loading of organics is relatively low in these strategies, which ultimately limited the practical energy density, especially the volumetric energy density. It is highly desirable to develop novel strategies to construct flexible electrodes with a high mass loading of organic active materials.

As a promising organic electrode material, perylene tetracarboxylic diimide (PTCDI) has demonstrated excellent electrochemical performances for Li^+/Na^+/K^+ ions storage, because of its functional carbonyl groups with the reversible enolization -C=O ↔ -C-O-M mechansim. [12-14] However, the low electrical conductivity and high dissolution in organic electrolytes result in unsatisfactory rate capability, poor cycle stability and eventually limited its practical applications. [15-17] Even though the polymerization strategy has been proposed to circumvent the dissolution phenomena, the conductivity of PTCDI for ion/electron transfer deteriorated inevitably. In addition, such attempt cannot tailor the mass loading of PTCDI onto substrate, failing in enhancing the energy density of devices. [16-18] Recently, we have developed an in-situ assembly strategy to efficiently deposit PTCDI nanofibers with optimized charge transport along the long axis on ITO surface. [19, 20] More impressively, the procedure of the layer by layer stacking facilitates the controllable formation of homogenous and compact of nanofibrous PTCDI networks. Inspiringly, we creatively deposit PTCDI nanofibers on soft ITO support via a molecular selfassembly strategy to form an unique flexible electrode with enhanced electrochemical performance such as larger specific capacity, higher rate capability and long cycling life due to the following advantages: (a) the increased intra/inter-molecular charge transport along the long axis of PTCDI nanofiber mediated by the effective intermolecular electron delocalization and short diffusion distance for interfacial ions owing to the tightly-ordered molecular self-assembly; [19, 20] (b) sufficient exposed surface with abundant active sites for charge storage and a strong adhesive force to anchor onto the substrate without any binder and conductive additives; (c) there is a good insolubility of the studied PTCDI in aqueous solution (for example: neutral sulfate solution and sulfuric acid solution) resulting in low shedding/dissolution probability of PTCDI nanofibers during cycle test. [20, 33] Furthermore, the reversible redox mechanism of PTCDI nanofiber during charge/discharge process is revealed via the integration of the in situ Raman

View Article Online
DOI: 10.1039/D0TA07267B

characterization and DFT calculation. Taking advantages of the safety of neutral aqueous electrolyte, excellent ionic conductivity, and the efficient dissolution suppression of PTCDI during charge/discharge cycling, we designed an AFSISD in which the flexible PICDI nanofiber and the activated carbon film are used as anode and cathode respectively. The fabricated AFSISD delivers a high energy density, power density and satisfactory cycling stability, outperforming nearly all previous aqueous hybrid devices. This study illustrates a facile selfassembly strategy to construct high-performance flexible electrodes using organic materials, providing a new method for the construction of wearable flexible electronic devices.

2. Experimental Section

2.1. Synthesis of PTCDI D-A Molecule. The PTCDI molecule (2,9-bis[1-[(1-methyl-4-piperidyl)methyl]]-3,4,9,10-perylene tetracarboxylic diimide) was synthesized following our previously reported literature as shown Figure S1 [19].

2.2. Synthesis of Activated Carbon (AC). Coconut shell charcoal (CSC, from AC Company in Jiangsu) and KOH (mass ration, CSC : KOH = 1:4) were mixed as carbon source and activator respectively, and activated at 800 ^{o}C for 1 h. When cooling down, washed it with 2 M HCl and deionized water respectively, to eliminate any metal residues totally. Finally, the obtained sample was dried at 80 ^{o}C for 24 h and labeled as AC.

2.3. Preparation of PTCDI D-A Nanofibers. PTCDI Nanofibers were formed by a solvent-vapor diffusion process, resulting in interfacial self-assembly on the surface of indium tin oxide (ITO) films, which served as the current collector. Specifically, a solid screw-cap containing 0.6 × 0.6 cm^2 ITO films was placed in a crystallizing dish, and 40 mL of methanol was injected to allow the screw cap to float on the methanol liquid.

View Article Online
DOI: 10.1039/D0TA07267B

Then, 80 µL PTCDI solution (1.0 mM PTCDI solution in chloroform) was slowly drop-cast onto the ITO surface, rapidly sealed and transferred to oven at 30 ^{o}C for 24 h. Finally, the nanofibers were dried in a vacuum oven at 50 ^{o}C for 60 min.

2.4. Material Characterization. The morphology, microstructure, and functional groups of PTCDI nanofibers were characterized SEM (Philips XL 30 instrument and a JEOL JSM-6700F microscope), FTIR (Bruker Vertex 70 FT-IR spectrometer) and micro-Raman spectra (LabRAM HR JY-Evolution, 532 nm). The porous structure of AC was characterized by Nitrogen adsorption/desorption isotherms, which were measured at 77 K with a Quadrachrome adsorption instrument. Before analysis, the samples were degassed at 200 ^{o}C for 24 h. The surface area was calculated according to the Brunauer-Emmett-Teller (BET) method.

2.5. The In-situ Raman Measurements. As can be seen from Figure S3, the test system mainly contains three parts. The computer is connected to the electrochemical workstation which is connected to the sample tank for cyclic voltammetry testing. Raman spectroscopy was used to real-time record the changes of chemical bond in the whole reaction process.

2.6. Electrodes Fabrication. For PTCDI nanofiber electrode, it was prepared as described in preparation of PTCDI nanofibers. The weight of PTCDI nanofiber is 0.05 mg and the active area is 0.36 cm^{2}. For AC electrode, it was prepared by mixing active material (80 wt % AC), conductive carbon (10 wt % Super P), and PVDF dissolved in N-methyl-2-pyrrolidone (NMP) (10 wt % PVDF). The mixed slurry was uniformly cast over the ITO films. The loading weight of AC is 0.8 mg and the active area is 0.36 cm^{2}. The obtained electrodes were dried under vacuum at 50 ^{o}C for 180 min.

2.7. Electrochemical Tests. The electrochemical measurements were carried out on an electrochemical workstation (CHI760E, Chenhua, China). The electrochemical tests of

View Article Online
DOI: 10.1039/D0TA07267B

half-cells were carried out using a three-electrode cell with platinum as counter electrode and Ag/AgCl as reference electrode. 1 M Na_2SO_4 solution was used as the electrolyte. Impedance spectra was measured at 0.1 Hz to 100 kHz frequency range with a 5 mV AC amplitude. Cyclic voltammetry was conducted in the -0.8 - 0.5 V range at increasing sweep rates from 1 to 1000 mV s^{-1}. Galvanostatic charge/discharge cycling was performed in the -0.9 - 0.1 V range at current densities in the 0.2 - 9.0 A g^{-1} range. The specific gravimetric capacitance (C_g) and areal capacitance (C_s) based on the galvanostatic discharge for three electrode system is calculated using equation (4) and (5):

$$C_g = \frac{I \times \Delta t}{M \times \Delta U} \qquad (4)$$

$$C_s = \frac{I \times \Delta t}{s \times \Delta U} \qquad (5)$$

Where I is the discharge current (A), M is the mass of the active materials (M_{PTCDI} = 0.05 mg) in electrode (g), s is the areal of active materials (s_{PTCDI} = 0.36 cm^2), ΔU (V) stands for the potential window within the discharge time Δt (s) after the ohmic drop. Full cell (PTCDI//AC) characterization was carried out in a two-electrode cell, PTCDI nanofibers as negative electrode was combined with AC as positive electrode with equivalent in capacity. Both electrodes were submerged in 1 M Na_2SO_4 aqueous electrolyte. Cyclic voltammetry was conducted in the 0-1.5 V range at increasing sweep rates from 1 to 100 mV s^{-1}. Galvanostatic charge-discharge experiments were carried out in the 0-1.46 V range at current densities in the 0.03-2.4 A g^{-1} range. The specific capacity ($C_{full\text{-}g}$ and $C_{full\text{-}s}$) and current density was calculated based on the total mass of both PTCDI and AC units in the full cell, and the calculation equation (6) and (7):

$$C_{full-g} = \frac{2 \times I \times \Delta t}{M \times \Delta U} \qquad (6)$$

$$C_{full-s} = \frac{2 \times I \times \Delta t}{S_{total} \times \Delta U} \qquad (7)$$

Where S_{total} is the total areal of active materials ($S_{total} = 0.72\ cm^2$). The specific energy density (E, Wh kg^{-1}) and specific power density (P, W kg^{-1}) for full cell (PTCDI//AC) were calculated by the equation (8) and (9):

$$E = \frac{C_{full-g} \times \Delta U^2}{2 \times 3.6} \qquad (8)$$

$$P = \frac{E \times 3600}{\Delta t} \qquad (9)$$

Where ΔU is the operation voltage ($\Delta U = U_{max}$ - IR drop), and Δt (s) is the discharge time. Moreover, volumetric energy density (E, mWh cm^{-3}) and volumetric power density (P, mW cm^{-3}) of the devices were gained according to the equation (10) and (11):

$$p = \frac{\Delta U \times I}{2 \times V} \qquad (10)$$

$$E = P \times t \qquad (11)$$

Where I (mA) is the applied current, V (cm^3) is the volume of the whole device (The areal and thickness of the PTCDI//AC are about $0.6 \times 0.6\ cm^2$ and 0.14 mm. Hence, the whole volume of the device is about 0.00504 cm^3), t (h) is the discharging time, ΔU (V) is the voltage window of GCD.

2.8. Computational Methodology. All density functional calculations covering geometry optimization and vibrational analysis were performed at theoretical level of Beck's 3-parameter Lee-Yang-Parr (B3LYP) with basis set Def2SVP as implemented in Gaussian 09 Rev. D01. All equilibrium geometries were confirmed by the absence of imaginary frequencies. The gas phase Gibbs free energy of sodium addition at 1 atm and 298 K was corrected with zero-point and thermal energies from the vibrational analysis. Table S3 is the cartesian coordinates of various PTCDI molecules.

3. Results and Discussions

3.1. Synthesis, Structure and Morphology Characterization

Figure 1a illustrates the schematic diagram for the fabrication of the flexible binder-free PTCDI electrodes. As shown, a cleaned ITO membrane which serves as a current collector is placed at the bottom of a shallow, wide, open container. Then the surface of ITO film is covered with a certain amount of the PTCDI stock solution (1 mM in chloroform). After that, the container is moved into a sealed vessel which contains methanol (poor solvent for PTCDI). Finally, following the solvent exchange which is driven by the vapor diffusion of methanol, the PTCDI molecules self-assemble into nano-fibrous framework to form electrodes via π-π molecular stacking forces gradually. As evidenced by SEM characterization in Figure 1b, the as-prepared PTCDI nanofibers fully cover on the surface of ITO, implying the success of this fabrication strategy. Detailed image discovers that the diameter and length of the PTCDI nanofibers are about 300 nm and up to 10 micrometers, respectively. It is impressive that these thin nanofibers interconnect each other to form networks with a strong adhesion to ITO substrate for efficient electron transfer. Additionally, this structural characteristic also reflects a large electrode/electrolyte interface and a shortened distance for sodium ion diffusion. Moreover, the structural evolution after assembly process was also discovered by spectra technologies. It is observed that PTCDI nanofibers present higher relative intensities than the PTCDI molecule, supporting the occurrence of ordered molecular organization during assembly (Figure 1c). In detail, besides the C-H in-plane bending vibrations (1300-900 cm^{-1}), the intensive absorption of C=C stretching at 1580 cm^{-1} and the strong C-N stretching at 1350 cm^{-1} indicate a large value of the dipole moment derivative. Impressively, the strong peaks at 1692 cm^{-1} and 1650 cm^{-1} can be ascribed to the antisymmetric in phase vibration and the out-of-phase symmetric stretching of C=O groups respectively, informing an abundant exposure of active sites for charge storage. Similarly, the C=O, C=C, C-H, Ring and Ring radical stretching

View Article Online
DOI: 10.1039/D0TA07267B

vibrations in PTCDI were also detected in Raman spectroscopy (Figure 1d). [21, 22] In short, all these structure characteristics indicate the successful self-assembly of PTCDI and the existence of C=O groups.

3.2. Electrochemical Characterization of PTCDI Nanofiber and Mechanism Exploration

To evaluate the electrochemical performance of PTCDI nanofiber electrodes, the galvanostatic charge-discharge (GCD) measurements were performed in 1 M Na_2SO_4 aqueous solution with a three-electrode system. It is observed in Figure 2a that the curves bend at ~-0.4 V in charging process and the discharging lines below -0.5 V are bent, implying the participation of redox reactions which might be caused by the reversible transformation between -C=O and -C-O-Na. That is, an oxidation reaction occurs at ~-0.4 V to convert -C=O to -C-O-Na, and a reduction reaction occurs at below -0.5 V to reduce -C-O-Na to -C=O during the discharge process. [12-20] Figure 2b presents the relationships between the specific capacitance values and charge/discharge current densities. Over the current density range from 0.1 A g^{-1} to 9 A g^{-1}, samples exhibit outstanding capacitive performance. For example, the calculated specific capacitance (SC) reached to 357, 204, 155, 134, 120, 108, and 103 F g^{-1} at the current density of 0.2, 0.4, 1, 2, 4, 5 and 9 A g^{-1}, respectively. The sluggish reduction in SC values suggests an enhanced rate performance. To further explore the kinetic process of Na^+ storage, the Cyclic Voltammograms (CVs) were carried out. As shown in Figure 2c, a pair of representative redox peaks are observed at similar potential regions during the CV scan at different rates (1-1000 mV s^{-1}). This phenomena indicates the reversible association/disassociation of Na^+ from PTCDI framework via the enolization reaction (-C=O $\leftrightarrow$-C-O-Na). To further reveal the kinetic information, the relationships between peak currents (i) and scan rates (ν) are presented as equation (1). [23-32]

View Article Online
DOI: 10.1039/D0TA07267B

$$i=a\nu^{b} \qquad (1)$$

Herein the values of a and b are variable. If the value of b is set as 0.5, the kinetic behavior is controlled by diffusion; if the value of b approaches to 1, it suggests that the surface-controlled pseudo-capacitive behavior is dominated. The value of b can be calculated from the linear relationship between log i and log ν. As displayed in Figure 2d, the values of b for cathodic and anodic peaks are almost equal to each other (0.8277 and 0.7961), further consolidating the satisfactory reversibility for sodium ion accumulation and release. In addition, these two values are close to 1, inferring the dominant contribution of the surface-controlled capacitive behavior. The diffusion and capacitive ratios were further estimated according to equation (2) [23-32]:

$$i=k_1\nu + k_2\nu^{1/2} \qquad (2)$$

Herein $k_1\nu$ and $k_2\nu^{1/2}$ stand for the current caused by the surface-controlled capacitive effect and the diffusion-controlled process respectively. The equation (2) can be further transformed into equation (3) [23-32]:

$$i/\nu^{1/2}=k_1\nu^{1/2} + k_2 \qquad (3)$$

The diffusion and capacitive ratios can be calculated by plotting $i/\nu^{1/2}$ vs. $\nu^{1/2}$ at various potentials. As shown in Figure 2e, about 67 % of the total current is derived from capacitive behavior even at 1 mV s^{-1}. Along with the increase of scan rates (1-100 mV s^{-1}), the capacitive contribution is gradually enhanced from 67 % to 99 % (Figure 2f). Furthermore, the EIS is employed to probe the interfacial contact between the electrode material and electrolyte in redox process (Figure S2). At very high frequencies, the intercept at real part (Z') is a combinational resistance of ionic resistance of electrolyte, intrinsic resistance of substrate and contact resistance at the active material/current collector interface (R_S). Here shows similar R_S values under different voltages (seen the inset). A major difference is the semicircle (the smaller the better) in the medium-

View Article Online
DOI: 10.1039/D0TA07267B

frequency range, which corresponds to the charge-transfer resistance (R_{CT}) caused by the Faradaic reactions. The R_{CT} depends on ion diffusion/transport in the electrolyte to electrode surface. [34, 35] The R_{CT} at redox potentials is smaller than that at OCV, implying a low ionic/charge transfer resistance between electrolyte and electrode interface, which can be also due to the tight adhesion of the self-assembled PTCDI nanofibers on ITO surface. Summarizing the results of the GCD, CV and EIS measurements, a desirable rate performance can be obtained from the self-assembly PTCDI nanofiber.

To further probe the structural evolution of PTCDI and the interior storage mechanism, the in-situ Raman spectroscopy was adopted with a three electrode configuration (Figure S3), taking advantages of its high sensitivity to organic species and its low scattering cross-section for water solvent. As depicted in Figure 3a and 3b, the in-situ Raman spectroscopy was recorded at different potential interval, during the charge/discharging cycle with a CV scan at 0.5 mV s^{-1}. The peak at 1698 cm^{-1} which is ascribed to the stretch of C=O group, disappears gradually during the oxidation reaction (the gray part in the Figure 3a) and slowly reappears as the reduction reaction proceeding (the blue part in the Figure 3a) within the potential range from 0.2 to -0.8 V, indicating the association/disassociation process of Na^+ via the reversible enolization reaction (-C=O↔-C-O-Na). Moreover, the appearance/disappearance of the characteristic peaks of ring radical (Na^+) of PTCDI at 818 and 728 cm^{-1} corresponding to the oxidation/reduction peak in the CV chart further consolidates this transformation reaction. Besides this reaction, the reversibility of structural transformation of PTCDI is also observed via the analyses of the C=C stretch and the ring stretch during charge/discharge process. In detail, the peaks at 1584 and 1573 cm^{-1} which are associated with the C=C stretch mode, shift positively to high wavenumber and merged

View Article Online
DOI: 10.1039/D0TA07267B

into one peak at 1599 cm^{-1}, accompanying with the appearance of a satellite peak at 1532 cm^{-1} during oxidating/charging. Reversibly, the peak at 1599 cm^{-1} split into two peaks of C=C at 1584 and 1573 cm^{-1} along with the fade of the satellite peak (1532 cm^{-1}) during the reducing/discharging. Additionally, the ring stretch peaks fluctuate in position and intensity (from 1378/1301 cm^{-1} to 1346/1245 cm^{-1}) during oxidating/charging and restore to the original state during reducing/discharging. This reversibility can also be verified by the cyclic CV experiments (Figure S6 and red lines in Figure 5b), wherein, the CV results show high recyclability at different scanning speeds (at low scan rate, the two-step single-electron redox shows two pairs of symmetrical redox peaks in Figure S6; while at high scan rate, it becomes a single-step two-electron redox, showing a pair of symmetrical redox peaks in Figure 5b), which further proved the reversibility of the structure and reaction. In conclusion, the in-situ Raman spectroscopy indicates the reversible transformation of the structure accompanying with the invertible enolization-reaction (-C=O↔-C-O-Na). In terms of molecular structure, four carbonyl groups exist in symmetric PTCDI molecule, which implies a maximum theoretical capacity of 176 mAh g^{-1} for Na^{+} accumulation. However, the actual capacity in our research is only about 110 mAh g^{-1}, which means that only half of the active sites make contributions to the energy storage. To elucidate this discrepancy in capacity and further explore the Na^{+} storage mechanism, density functional theory (DFT) calculations were carried out. PTCDI monomers were investigated at theoretical level of Beck's 3-parameter Lee-Yang-Parr (B3LYP) with basis set Def2SVP as implemented in Gaussian 09 Rev. D01. It is carried out by simulating the carbonyl reaction at different positions (the carbonyl-positions are numbered 1, 2, 3, 4 in a clockwise direction). As can be seen in Figure 4a, there are six simulated structures of reactions, namely 1, 1-2, 1-3, 1-4, 1-2-3, 1-2-3, among which two equivalent Na^+ storage by two carbonyl groups (1-2, 1-3, 1-4) shows lower Gibbs free energy (ΔG), especially the para-reaction has the smallest Gibbs free energy ($\Delta G=$ -70 kcal). This can indicate that the para-carbonyl reaction has the greatest spontaneity. In addition, the carbonyl reactions at positions 1-2 and 1-3 have higher and similar absolute band gap energy, indicating that the products of the reactions at positions 1-2 and 1-3 have relative structural stability. Considering the common influence of Gibbs free energy and absolute band gap energy, it is concluded that the carbonyl reaction products at 1-2 and 1-3 positions coexist, of which the products in 1-3 sites are the main ones. Therefore, the actual capacity is smaller than the theoretical capacity by the simultaneous reaction of four carbonyl groups. [27-29] Furthermore, the energy comparison of LUMO and HOMO orbitals of PTCDI monomer and dimer was presented in Figure 4b. The LUMO/HOMO levels of PTCDI monomer and dimer were calculated to be -2.64/-2.98 eV, -2.48/-3.15 eV, yielding the absolute energy gaps of 0.34 and 0.67 eV for PTCDI monomer and dimer, respectively. The higher value indicates the assembled PTCDI aggregates are more stable than monomer due to strong π-π interaction. [19, 20, 27-30] According to the above calculation and the observation in Raman spectra, we proposed the sodium ion storage mechanism as Figure 4c.

3.3. Electrochemical Characterization of the Integrated Full Cell

To further assess their practical application in flexible electronics, an AFSISD is fabricated, where the PTCDI nanofiber and flexible activated carbon (AC) in Figure 5a act as negative electrode and positive electrode respectively. It is envisioned that the utilization of PTCDI will ensure the device with a large specific capacitance and correlated high energy density, and the participation of AC will promise the device with excellent rate performance, satisfactory power density as well as long cycling life. To determine the cut off voltage of AFSISD, the CVs of PTCDI nanofiber and AC are overlapped in Figure 5b. Different from the surface-controlled pseudo-capacitance of Na^+ for PTCDI nanofiber, a typical double layer capacitance behavior from adsorption/desorption of SO_4^{2-} ions is found for AC by virtue of its high surface area (2455.8 m^2 g^{-1}) and abundant porosity (Figure S4 and Table S1). It is deduced that the maximal cut off voltage for the AFSISD can reach to 1.46 V. Moreover, a pair of conspicuous peaks are observed in CV curves at different scan rates, implying the occurrence of redox reactions during energy storage (Figure 5c). In addition, the GCD plots demonstrate an enhanced power density (Figure 5d), for example, the fabricated AFSISD can charge within 35 s at a current density of 2.4 A g^{-1}. As demonstrated in Figure 5e and 5f, the maximal mass and areal specific capacitance in full cell reached to 280 F g^{-1} and 241 mF cm^{-2}, respectively, which are higher than those of AC//AC capacitors as shown in Table S2. Most importantly, benefitting from the cooperation of PTCDI and AC, the AFSISD demonstrates a satisfactory energy and a remarkable power density. As displayed in Figure 5g and 5h, the Ragone plots discover the overall performance of devices in terms of energy density and power density. It can be seen that the maximal mass energy density of 83.8 Wh kg^{-1} and the maximal power density of 3.4 kW kg^{-1} are achieved. The maximal volumetric energy and power densities are 7.1 mWh cm^{-3} and 289.7 mW cm^{-3}, respectively. Furthermore, Figure 5i demonstrates the relationship between imaginary capacitance and frequency in electrochemical impedance spectroscopy. A sharp peak and a max capacitance $C''(\omega)$ are obtained at a frequency of f_0 which refers the relaxation time as $\tau_0=1/f_0$. The minimum τ_0 is about 7.46 s. This relaxation time manifests the shortest time needed to discharge all the energy from this energy storage device equipped with an efficiency of >50 %. [31, 32] The lower relaxation time also indicates improved power density. Moreover, more than 80 % capacity retention was obtained at a rapid current density of 0.06 A g^{-1} after 1000 cycles, demonstrating an outstanding cycling stability (Figure S5, Supporting Information). Finally, the performance was compared with other similar devices. It can be observed from Table S2 (Supporting Information) that the PTCDI nanofiber//AC device presents desirable overall performance among several proposed aqueous energy storage devices. Such a combination to realize higher energy density and higher power density is expected to bridge the gap between battery-level energy density and supercapacitor-level power density in wearable electronics.

To be used as flexible energy storage devices for powering wearable electronics, mechanical flexibility tests are necessary. As shown in the schematic diagram in Figure 6a, a flexible quasi-solid-state AFSISD was constructed as a sandwich structure with PTCDI-nanofiber cathode, AC anode, and poly(vinyl alcohol) (PVA)-Na_2SO_4 gel electrolyte. Figure 6b exhibits the CV curves of the device at different bending angles, displaying almost imperceptible changes in the coverage areas of the CV curves. Figure 6c shows the galvanostatic charge/discharge curves for the belt-shaped AFSISD under different bending conditions (initial flat, bending to 45^o, 90^o, 135^o, 180^o and a circle to re-flat), only minor capacity change occurred under different bending conditions. The corresponding cycling stability results are presented in Figure 6d. It can be seen that the belt-shaped AFSISD lost a little receivable capacity with repeated bending angle and continuous different bending operation, which can be attributed to the fact that repeated bending destroyed the tight contact of the anode, separator, and cathode gradually resulting in an increased impedance of the battery. Importantly, the little loss of capacity also demonstrates good flexibility and strong mechanical properties against repeated bending.

4. Conclusions

View Article Online
DOI: 10.1039/D0TA07267B

In conclusion, the PTCDI nanofiber negative electrode was prepared via a facile self-assembly strategy. The reversible Na^+ storage mechanism and structural changes for PTCDI nanofiber was revealed by combining the electrochemical analysis of in-situ Raman spectroscopy and DFT computation. The pseudo-capacitive behavior based on the reversible enolization -C=O ↔ -C-O-Na was demonstrated. The as-prepared PTCDI nanofiber electrode presents desirable Na^+ storage performance, achieving a high capacitance of 357 F g^{-1} at a current density of 0.2 A g^{-1}. Furthermore, a hybrid sodium ion device based on PTCDI nanofiber as anode and AC as cathode was constructed, displaying higher mass energy density (83.8 Wh kg^{-1}) and power density (3.4 kW kg^{-1}), and desirable volumetric energy and power densities (7.1 mWh cm^{-3} and 289.7 mW cm^{-3}). Meanwhile, our devices display admirable mechanical flexibility enough to sustain various bending. This work not only push forward the exploration of the fexible organic electrodes for energy storage applications, but pioneer research on morphological design for AFSISDs.

Conflict of Interest

The authors declare that they have no conflict of interests.

Acknowledgements

This work was financially supported by the “Western Light” Foundation of Chinese Academy of Sciences (Grant No. 2019-XBQNXZ-A-002), the National Natural Science Foundation of China (Grant No. 51663016), the Youth Innovation Promotion Association, Chinese Academy of Sciences (Grant No. 2019427), the Xinjiang Science Foundation for Distinguished Young Scholars and the Xinjiang Program of Introducing High-Level Talents.

View Article Online
DOI: 10.1039/D0TA07267B

Appendix A. Supplementary materials

Supplementary materials to this article can be found online.

References

[1] Arico AS, Bruce P, Scrosati B, et al. Nanostructured materials for advanced energy conversion and storage devices. Nat Mater 2005; 4: 366-367.

[2] Dunn B, Kamath H, Tarascon JM. Electrical energy storage for the grid: A battery of choices. Science 2011; 334: 928-935.

[3] Guo YG, Hu JS, Wan LJ. Nanostructured materials for electrochemical energy conversion and storage devices. Adv Mater 2008; 20: 2878-2887.

[4] Larcher D, Tarascon, JM. Towards greener and more sustainable batteries for electrical energy storage. Nat Mater 2015; 7: 19-29.

[5] Augustyn V, Simon P, Dunn B. Pseudo-capacitive oxide materials for high-rate electrochemical energy storage. Energy Environ Sci 2014; 7: 1597-1614.

[6] Palomares V, Serras P, Villaluenga I, et al. Na-ion batteries, recent advances and present challenges to become low cost energy storage systems. Energy Environ Sci 2012; 5: 5884-5901.

[7] Dong X, Chen L, Su X, et al. Flexible aqueous lithium-ion battery with high safety and large volumetric energy density. Angew Chem Int Ed 2016; 55: 7474-7477.

[8] Ding J, Wang HL, Li Z, et al. Update on Na-based battery materials: A growing research path. Energy Environ Sci 2013; 6: 2312-2337.

[9] Häupler B, Wild A, Schubert US. Carbonyls: powerful organic materials for secondary batteries. Adv Energy Mater 2015; 5: 1402034.

[10] Liang Y, Tao Z, Chen J. Organic electrode materials for rechargeable lithium batteries. Adv Energy Mater 2012; 2: 742-769.

[11] Lu Y, Hou X, Miao L, et al. Cyclohexanehexone with ultrahigh capacity as cathode materials for lithium-ion batteries. Angew Chem Int Ed 2019; 58: 7020-7024.

[12] Zhao L, Zhao J, Hu YS, et al. Disodium Terephthalate ($Na_2C_8H_4O_4$) as high performance anode material for low-cost room-temperature sodium-ion battery. Adv Energy Mater 2012; 2: 962-965.

[13] Hernandez G, Casado N, Zamarayeva AM, et al. Perylene polyimide-polyether anodes for aqueous all-organic polymer batteries. ACS Appl Energy Mater 2018; 1: 7199-7205.

[14] Wang C, Tang W, Yao Z, et al. Potassium perylene-tetracarboxylate with two-electron redox behaviors as a highly stable organic anode for K-ion batteries. Chem Commun 2019; 55: 1801-1804.

[15] Sun X, Wang C, Gong Y, et al. A flexible sulfur-enriched nitrogen doped multichannel hollow carbon nanofibers film for high performance sodium storage. Small 2018; 14: 1802218.

[16] Wang Z, Li H, Tang Z, et al. Hydrogel electrolytes for flexible aqueous energy storage devices. Adv Funct Mater 2018; 28: 1804560.

[17] Li H, Peng L, Zhu Y, et al. Achieving high-energy–high-power density in a flexible quasi-solid-state sodium ion capacitor. Nano Lett 2016; 16: 5938-5943.

[18] Pushparaj VL, Shaijumon MM, Kumar A, et al. Flexible energy storage devices based on nanocomposite paper. PNAS 2007; 104: 13574-13577.

[19] Chen S, Slattum P, Wang C, et al. Self-assembly of perylene imide molecules into 1D nanostructures: methods, morphologies, and applications. Chem Rev 2015; 115: 11967-11998.

[20] Yang L, Wang M, Slattum PM, et al. Donor-acceptor supramolecular organic nanofibers as visible-light photoelectrocatalysts for hydrogen production. ACS Appl Mater Interfaces 2018; 10: 19764-19722.

[21] Brown KE, Veldkamp, BS Co DT, et al. Vibrational dynamics of a perylene-perylenediimide donor-acceptor dyad probed with femtosecond stimulated Raman Spectroscopy. J Phys Chem Lett 2012; 3: 2362-2366.

[22] Angelella M, Wang C, Tauber MJ. Resonance Raman spectra of a perylene bis(dicarboximide) chromophore in ground and lowest triplet states. J Phys Chem A 2013; 117: 9196-9204.

[23] Kim HS, Cook JB, Lin H, et al. Oxygen vacancies enhance pseudocapacitive charge storage properties of MoO_{3-x}. Nat Mater 2017; 16: 454-460.

[24] Stevenson KJ, Ozolins V, Dunn B. Electrochemical energy storage. Acc Chem Res 2013; 46: 1051-1052.

[25] Brezesinski T, Wang J, Tolbert SH. Ordered mesoporous alpha-MoO_3 with iso-oriented nanocrystalline walls for thin-film pseudocapacitors. Nat Mater 2010; 9: 146-151.

[26] Augustyn V, Come J, Lowe MA, et al. High-rate electrochemical energy storage through Li^+ intercalation pseudocapacitance. Nat Mater 2013; 12: 518-522.

[27] Zindy N, Blaskovits JT, Beaumont C, et al. Pyromellitic diimide-based copolymers and their application as stable cathode active materials in lithium and sodium-ion batteries. Chem Mater 2018; 30: 6821-6830.

[28] Zindy N, Aumaitre C, Mainville M, et al. Pyrene diimide based pi-conjugated copolymer and single-walled carbon nanotube composites for lithium-ion batteries. Chem Mater 2019; 31: 8764-8773.

[29] Wang J, Shi W, Liu D, et al. Supramolecular organic nanofibers with highly efficient and stable visible light photooxidation performance. Appl Catal B 2017; 202: 289-297.

[30] Chen D, Avestro AJ, Chen Z, et al. A rigid naphthalenediimide triangle for organic rechargeable lithium-ion batteries. Adv Mater 2015; 27: 2907-2912.

[31] Biswal M, Banerjee A, Deo M, et al. From dead leaves to high energy density supercapacitors. Energy Environ Sci 2013; 6: 1249-1259.

[32] Yin J, Zhu Y, Yue X, et al. From environmental pollutant to activated carbons for high-performance supercapacitors. Electrochim Acta 2016; 201: 96-105.

[33] Zhang Z, Wang J, Liu D, et al. Highly efficient organic photocatalyst with full visible light spectrum through π–π stacking of TCNQ–PTCDI. ACS Appl Mater Interfaces 2016; 8: 30225-30231.

[34] Wei N, Ruan L, Zeng W, et al. Compressible supercapacitor with residual stress effect for sensitive elastic-electrochemical stress sensor. ACS Appl Mater Interfaces 2018; 10: 38057-38065.

[35] Ma Y, Wei N, Wang Q, et al. Ultrathin PEDOT: PSS/rGO aerogel providing tape-like self-healable electrode for sensing space electric field with electrochemical mechanism. Adv Electron Mater 2019; 5: 1900637.

View Article Online
DOI: 10.1039/D0TA07267B

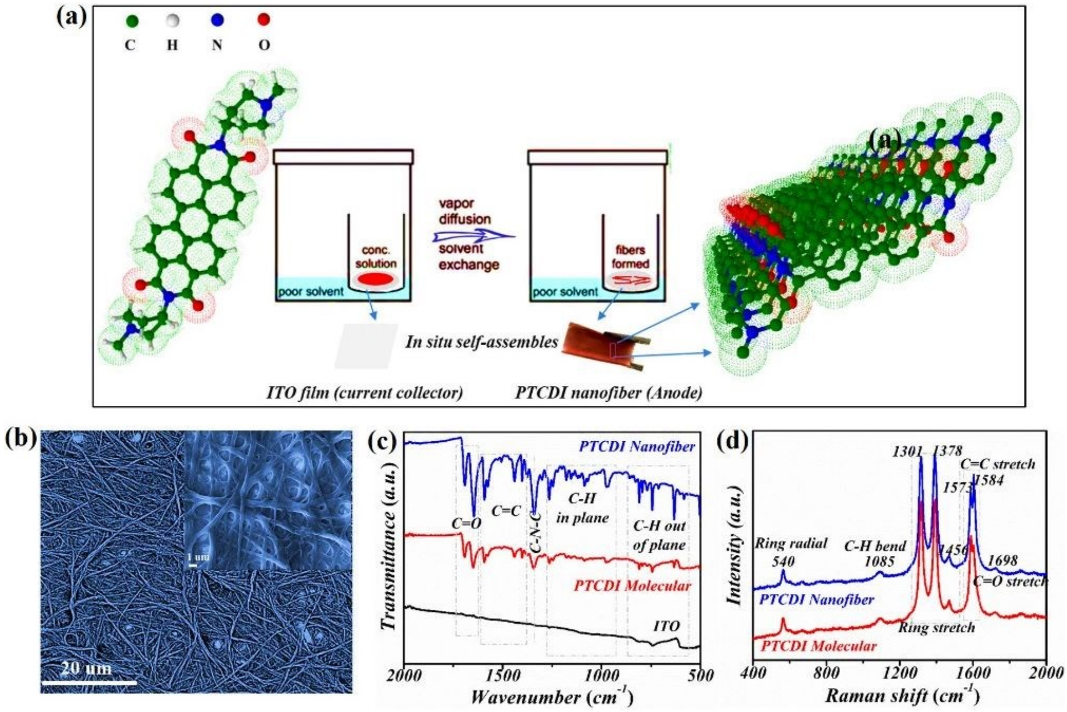

Figure 1. (a) The schematic diagram for the fabrication of the flexible binder-free PTCDI electrodes. (b) SEM images of PTCDI nanofibers. (c) FTIR and (d) Raman spectroscopy of PTCDI.

View Article Online
DOI: 10.1039/D0TA07267B

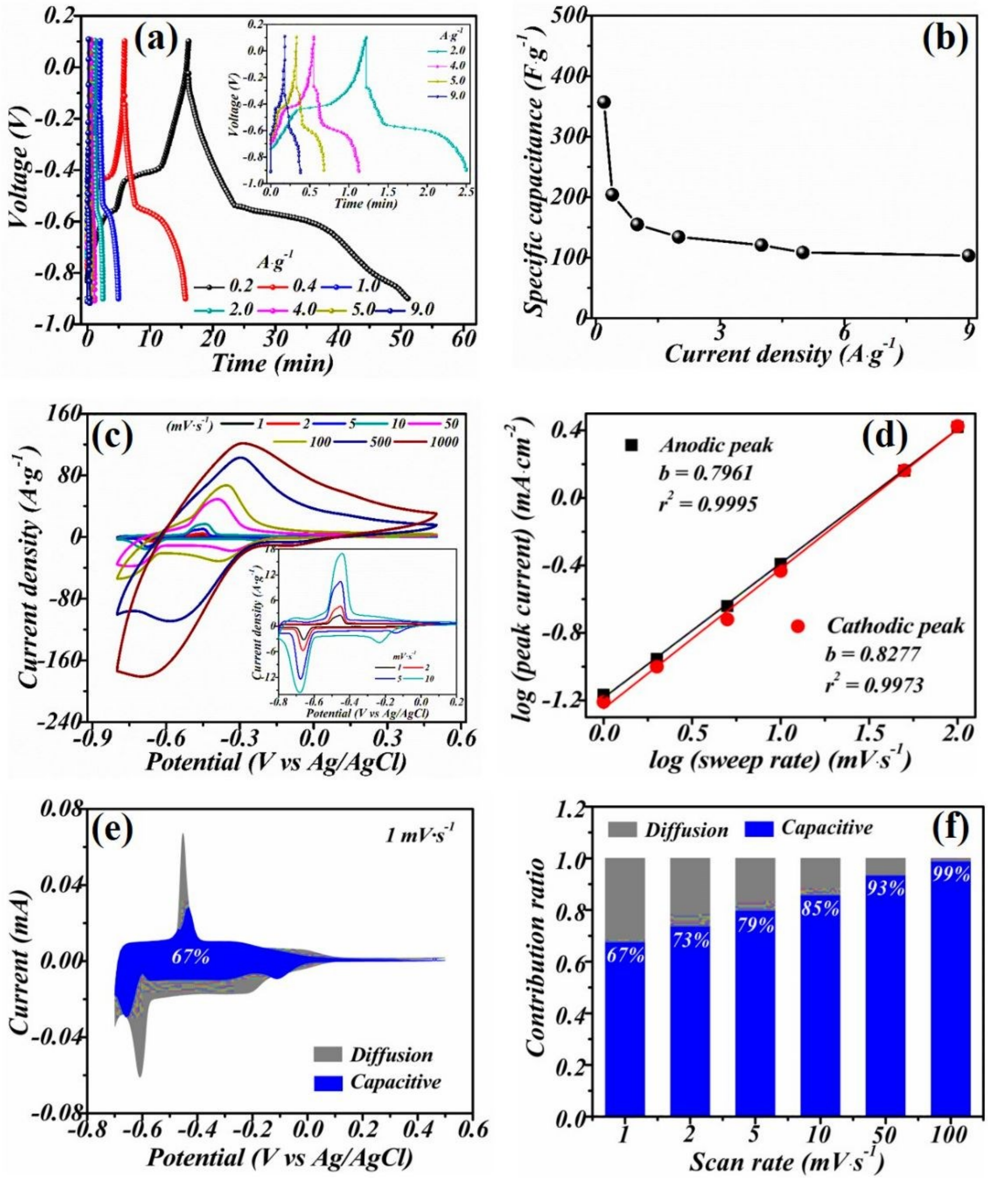

Figure 2. (a) GCD measurements of PTCDI nanofiber electrode at different current densities in 1 M Na_2SO_4 aqueous electrolyte. (b) The relationships between specific capacitances and applied current densities. (c) CV plots of PTCDI nanofiber electrode at different sweep rates from 1 to 10000 mV s^{-1}. (d) b values calculated from the relationships between the scan rates and peak currents. (e) The proportions of capacitive and diffusion currents in PTCDI nanofiber electrode at the scan rate of 1 mV s^{-1}. (f) The percentages of capacitive and diffusion-controlled contributions at various sweep rates.

View Article Online
DOI: 10.1039/D0TA07267B

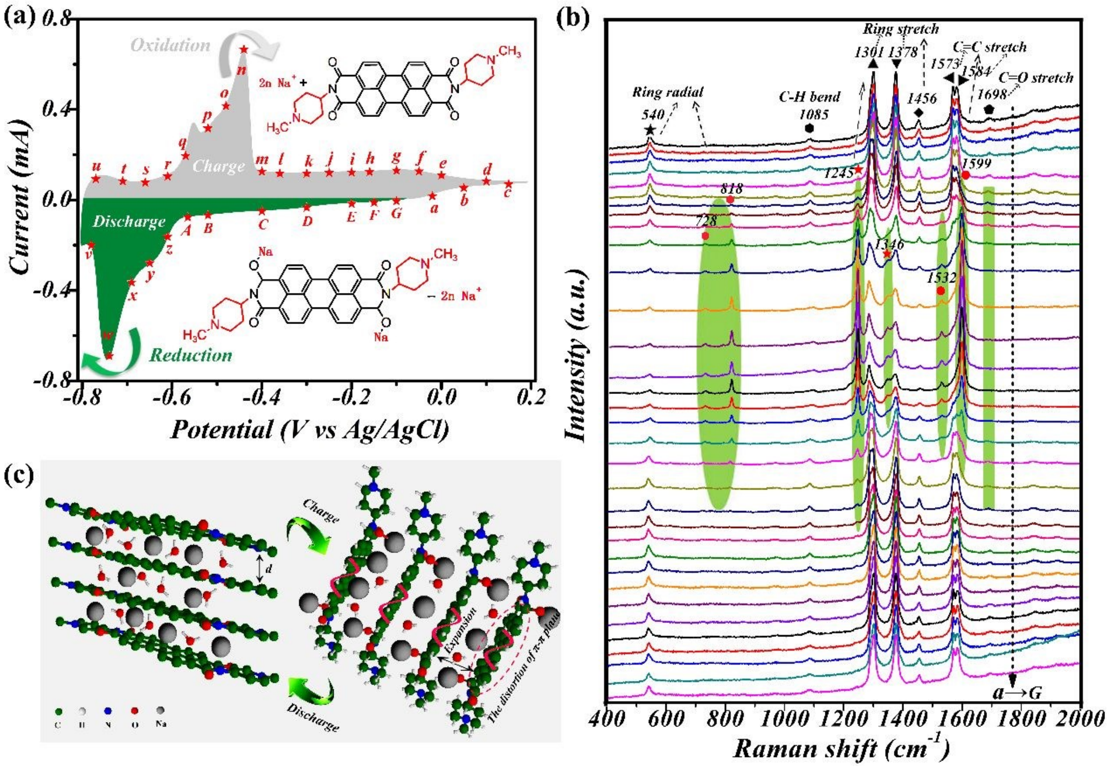

Figure 3. (a) CV curve of PTCDI nanofiber electrode at a scan rate of 0.5 mV s^{-1} in 1 M Na_2SO_4 aqueous electrolyte. (b) The corresponding in situ Raman spectroscopic evolution of PTCDI nanofiber electrode at different applied potentials in CV measurement. (c) The possible structure variations of PTCDI framework along with the association of Na^+.

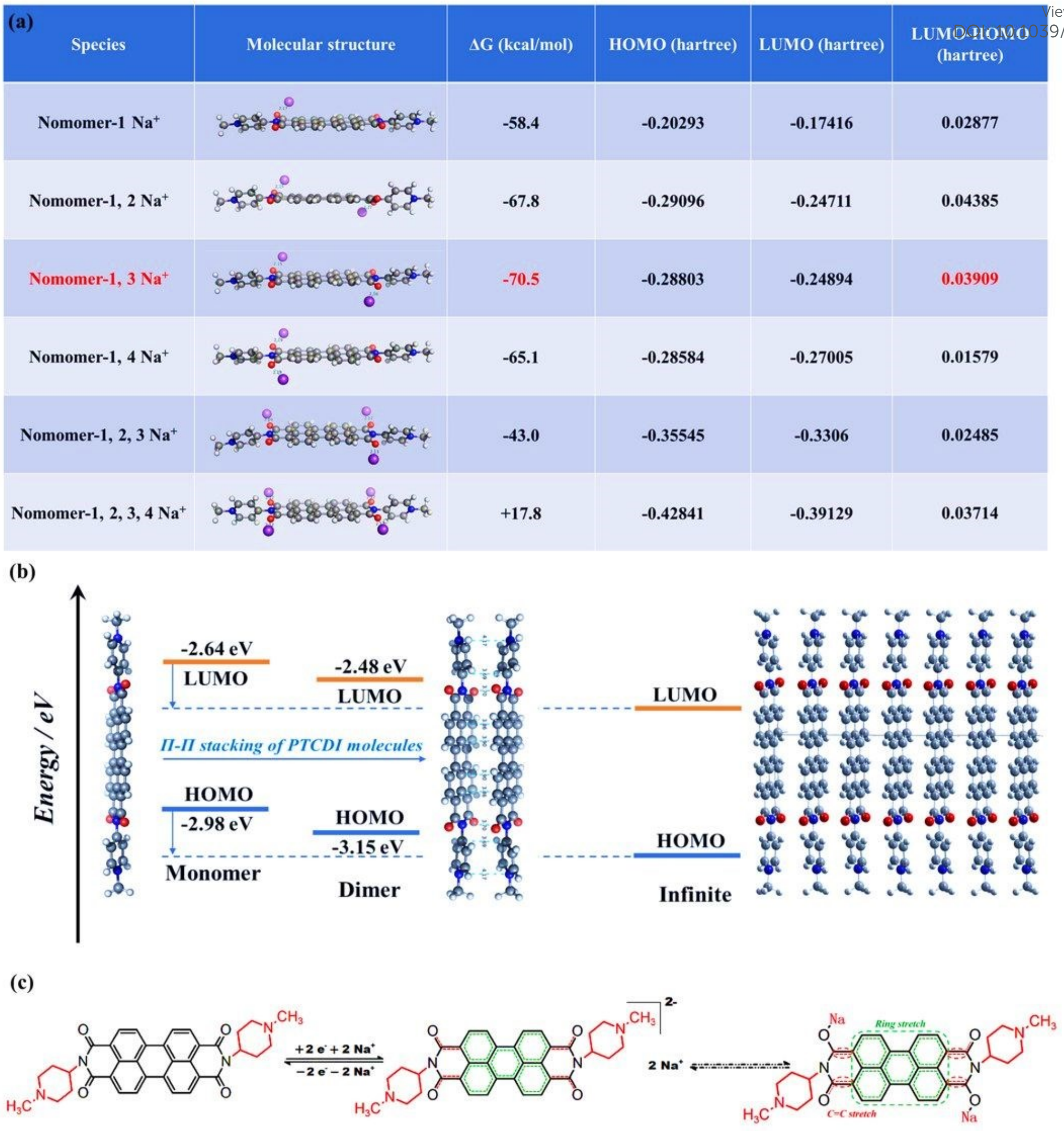

(a)

Species	Molecular structure	ΔG (kcal/mol)	HOMO (hartree)	LUMO (hartree)	LUMO-HOMO (hartree)
Nomomer-1 Na^+		-58.4	-0.20293	-0.17416	0.02877
Nomomer-1, 2 Na^+		-67.8	-0.29096	-0.24711	0.04385
Nomomer-1, 3 Na^+		-70.5	-0.28803	-0.24894	0.03909
Nomomer-1, 4 Na^+		-65.1	-0.28584	-0.27005	0.01579
Nomomer-1, 2, 3 Na^+		-43.0	-0.35545	-0.3306	0.02485
Nomomer-1, 2, 3, 4 Na^+		+17.8	-0.42841	-0.39129	0.03714

Figure 4. (a) Gibbs free energies of different reduction sites for PTCDI monomer. (b) Energy comparison of HOMO and LUMO orbitals of PTCDI monomer and dimer. (c) The possible Na^+ storage mechanism of the PTCDI nanofiber electrode.

View Article Online
DOI: 10.1039/D0TA07267B

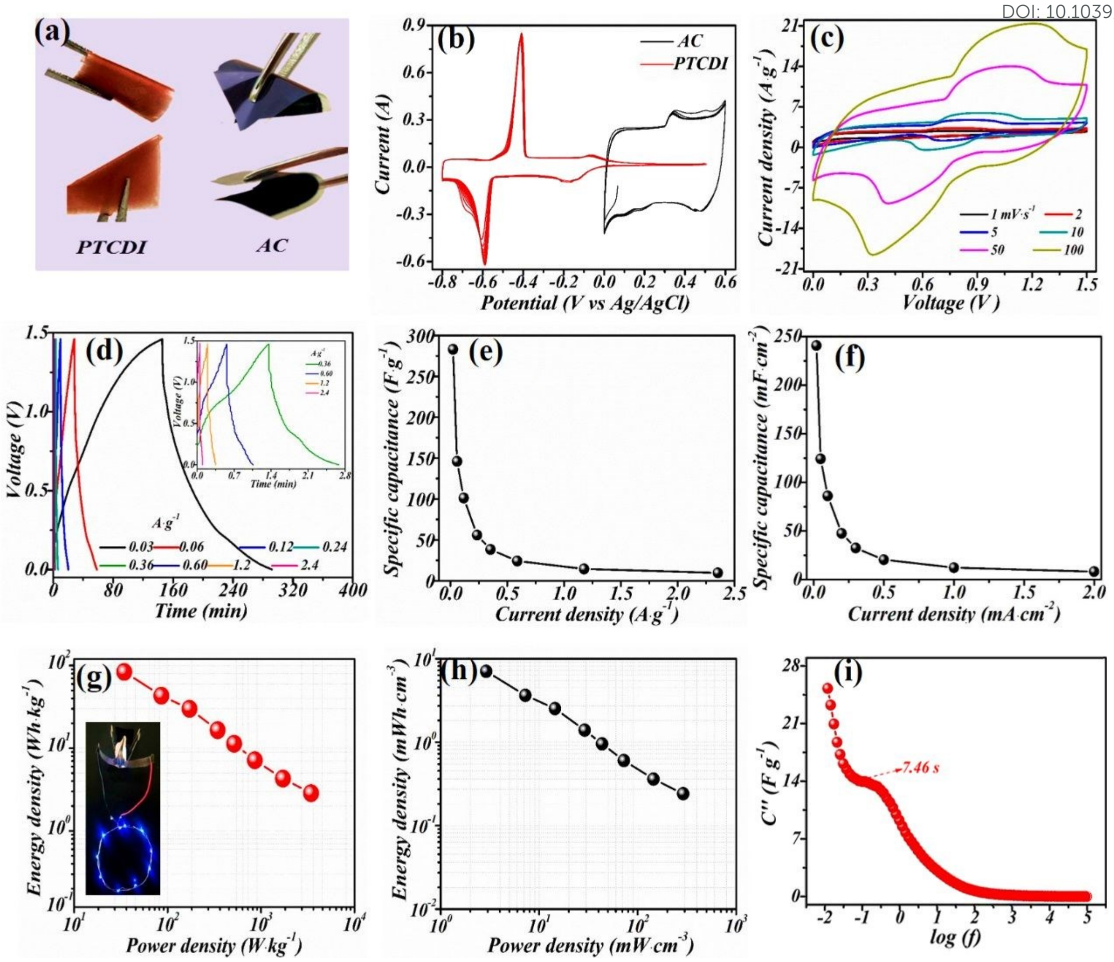

Figure 5. (a) Photo images of flexible PTCDI nanofiber electrode and AC electrode. (b) The overlapped CV curves of PTCDI nanofiber electrode and AC electrode at a scan rate of 5 mV s^{-1} in 1 M Na_2SO_4 aqueous electrolyte. (c) The CV curves of PTCDI nanofiber//AC device at electrode at various scan rates from 1 to 100 mV s^{-1}. (d) GCD measurements of device at different current densities from 0.03 to 2.4 Ag^{-1} (total mass of cathode and anode was used to calculate current density). (e) The relationships between mass specific capacitance and applied current density for FSISD. (f) The relationships between areal specific capacitance and applied current density for FSISD. (g) and (h) Ragone plots of FSISD. (i) Frequency dependent imaginary capacitance plot.

View Article Online
DOI: 10.1039/D0TA07267B

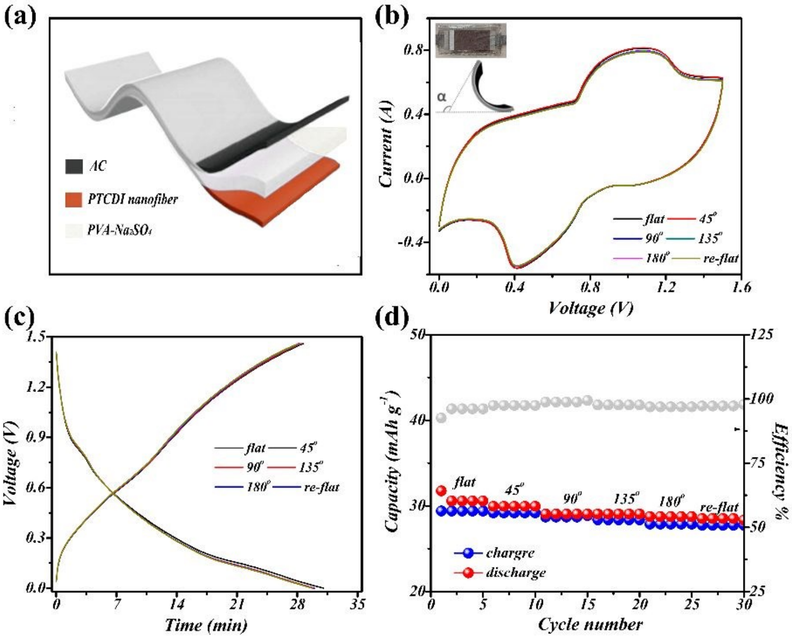

Figure 6. (a) Schematic illustration of the assembled FSISD; (b) CV curves at a scan rate of 2 mV s^{-1} and (c) the galvanostatic discharge/charge curves of the belt-shaped FSISD at different angles; (d) Cycle stability at successive various repeated bending states at a current density of 0.6 A g^{-1}.